Full Length Research Paper

Impacts of surface wave-induced Coriolis-Stokes forcing on the upper ocean circulation

Zengan Deng[1,2]*, Guijun Han[1,2], Xuefeng Zhang[1,2] and Kejian Wu[3]

[1]Key Lab of Marine Environmental Information Technology, SOA, Tianjin 300171, China.
[2]National Marine Data and Information Service, Tianjin 300171, China.
[3]Ocean University of China, Qingdao 266100, China.

Using the Hybrid Coordinate Ocean Model (HYCOM), six experiments configured for three different domains: Global Ocean, South China Sea (SCS) and Western North Atlantic Ocean (WNA), are designed to investigate the effects of wave-induced Coriolis-Stokes forcing (CSF) on ocean surface phenomena including circulation, temperature and mixing processes. CSF calculated using wave parameters simulated by the WaveWatch III (WW3) model, which is used as a part of the driving force for HYCOM. The results indicated that: 1) CSF does not fundamentally change the circulation pattern in the upper ocean mixed-layer (ML), 2) over most of the global ocean, the direction of Stokes transports ($\vec{T}_S$) is different from that of the changes in depth-integrated current transports ($\Delta \vec{T}_c$) caused by CSF, 3) the monthly-mean $\Delta \vec{T}_c$ in the ML varies from month to month in both direction and magnitude, and the CSF plays a more significant role in regions of intensive gyre, such as the area near Yucatan Channel, than in regions of weak currents, 4) both Sea Surface Temperature (SST) and Mixed-Layer Depth (MLD) are noticeably influenced by the CSF.

Key words: Coriolis-Stokes forcing, upper ocean mixed layer, currents, stokes transport.

INTRODUCTION

The motion of the ocean surface water has been investigated extensively for its critical role in transportation of momentum, mass and energy as well as in air-sea interaction. Two main types of motion exist in the upper ocean: waves and currents. Ocean surface waves have three main effects on turbulence in the ocean surface mixed-layer (ML), that is wave breaking, Langmuir circulations (McWilliams et al., 1997; Teixeira and Belcher, 2002; Kantha and Clayson, 2004; Carniel et al., 2005; Ardhuin and Jenkins, 2006), and Coriolis-Stokes Forcing (hereinafter referred to as CSF) (Hasselmann, 1970; Huang, 1979; McWilliams et al., 1999; Polton et al., 2005). Interaction of turbulent vorticity with Stokes drift results in Langmuir circulations, while interaction of large-scale planet vorticity with Stokes drift produces CSF which can be understood by a divergence of the wave-induced stress (Hasselmann, 1970). Both wave breaking and Langmuir circulations serve as additional sources of Turbulent Kinetic Energy (TKE) in the upper ocean (Ardhuin and Jenkins, 2006), whereas CSF changes the upper layer dynamics by acting on the momentum equation. Kantha and Clayson (2004) and Carniel et al. (2005) included the Stokes production into turbulence models, and found that the wave-induced source term extracts energy from wave motions and transfers it into turbulence which then consequently results in changes in upper layer properties, such as temperature and velocity. However, the large-scale CSF has never been implemented in a three-dimensional numerical model for real ocean simulating, thus there is a need to do so.

In the absence of surface wind stress, the ocean surface currents are mainly attributed to pure Stokes drift induced by waves (Bye, 1967; Kenyon, 1970). The ocean surface Stokes drift velocity increases linearly with increasing wind speed, and contributes significantly to the

---
*Corresponding author. E-mail: dengzengan@gmail.com.

total mean surface currents in the ocean (Kenyon, 1970). Korvin-Kroukovsky (1972) and Ianniello and Garvine (1975) calculated the Stokes and Ekman drift separately, and both found that the wave-induced drift is dominant in their uncoupled model. Hasselmann (1970) found that the interaction between the planetary vorticity and the Stokes drift produces a forcing on Eulerian momentum balance known as CSF. Huang (1979) demonstrated that, the CSF changes the usual Ekman balance in the wind-driven mixed-layer (ML) and the current profiles in combination with Coriolis forcing and the divergence of vertical momentum transfer by turbulent stress. Based on field observations and theoretical analysis, Huang (1979) concluded that any model of the surface drift, currently neglecting the contribution of wave motion would be incomplete. The study of McWilliams and Restrepo (1999) showed that, the wave-driven current effects sometimes could be significant in the basin-scale circulation compared with the wind-driven counterpart. Polton et al. (2005) suggested that, according to the observations of the Ekman current profile, Stokes drift might dynamically influence the current profile. By comparing his research results with observations, he concluded that the changes of the current profile due to CSF are consistent with the differences between observations and the classical Ekman profile. He also showed that the current profile could be influenced by CSF throughout the Mixed-Layer Depth (MLD) by changing the effective boundary condition on the standard wind-driven Ekman solution. Recently, Deng et al. (2007, 2009) estimated the wave-induced Stokes transport over the Pacific by using ECMWF data and the wave parameters simulated by the WaveWatch III (WW3), and noticeable swell transports are found over the Eastern Pacific. These studies also suggested that, the Stokes drift over the Eastern Pacific originates from the Westerlies and contributes to the basin-wide ocean circulation. Over all, CSF induces the momentum transfer between currents and waves, thus changes current field and temperature gradient in the upper ocean.

In order to estimate the effect of CSF, numerical method is used in this work. Sensitivity experiments are conducted using a HYCOM-WW3 one-way coupling model over the global ocean, South China Sea (SCS) and Western North Atlantic Ocean (WNA) region, respectively. Some background knowledge of SCS and WNA will be given in the following. [5]SCS is the largest semi-enclosed marginal sea (3.5×10^6 km^2) in the west Pacific Ocean. It has a shallow shelf in the south, the Vietnamese-Chinese coast to the north, and a deep basin at the center. A chain of islands separates SCS from adjacent oceans. SCS is connected to East China Sea through Taiwan Strait, to Pacific Ocean through Luzon Strait which is the deepest strait with maximum depth of 2400 m, to Sulu Sea via the Mindoro Strait, to Indian Ocean through the Strait of Malacca, and to Java Sea through the Karimata and Gasper Straits. The topography of SCS is complicated, and the shelf that extends from the Gulf of Tonkin to Taiwan Strait is about 70 m in depth and 150 km in width. The Sunda Shelf which links SCS to Malaysia, Southeast Asia, Sumatra, Java and Borneo, is a submerged passage with 100 m depth in the middle. The depth of the center of Thailand Gulf is about 70 m. In the interior, the deep basin is 1100 km southeast-northwest and 1800 km northeast-southwest.

One of the striking characteristics of SCS is the seasonally reversing monsoon winds that are important in driving the upper ocean circulation. The weaker southwesterly summer monsoon winds have a wind stress of over 0.1 Nm^{-2} from April to August, and the stronger northeasterly winter monsoon winds correspond to a maximum wind stress of approximately 0.3 Nm^{-2} from November to March (Chu et al., 1999). Many studies about SCS have been carried out previously by different researchers. Shaw and Chao (1994) demonstrated that the northward jet in summer flows away from the coast of Vietnam at about 12°N and the southward jet in summer moves along the western boundary. A series of numerical experiments conduced by Metzger and Hurlburt (1996) suggested that, the local monsoon has little effect on the circulation of SCS and it is just a function of model geometry and large-scale forcing over the Pacific. Qu et al. (1999) investigated the upper-layer circulation by using all available historical temperature data combined with climatological temperature-salinity relationships but without winds in the SCS, and they revealed that two cyclonic eddies, namely, the West Luzon eddy and the East Vietnam eddy exist at around 18°N, 118°E from late fall to early spring coinciding well with a positive wind stress curl both in location and time and at about 14°N, 110°E from late summer to early fall. Chu et al. (1999) found that during the summer (winter) monsoon period, the SCS surface circulation is generally anti-cyclonic (cyclonic) with a strong western boundary current, the Vietnam coastal jet, which moves northward (southward) during summer (winter) with a mean maximum speed of 0.5 ms^{-1} (0.95 ms^{-1}), and a mean volume transport of 5.5 Sv (10.6 Sv) extending to a depth of around 200 m (500 m).

The second experiment domain (WNA) consists of the Gulf of Mexico, Caribbean Sea and part of the western North Atlantic Ocean. The Gulf of Mexico is a semi-enclosed sea that connects in the south to the Caribbean Sea through the Yucatan Channel, and in the east to the Atlantic Ocean through the Strait of Florida. The Gulf has a central basin (about 3500 m in depth) of relatively limited extent (about 90°~94°W and 23°~25°N), surrounded by continental rise, slope and shelves (Oey et al., 2005). The circulation of WNA region, especially of the Gulf of Mexico region, has been well studied in the past decades for its dominant flow feature of the Caribbean Current in the Caribbean Sea, the Loop Current in the Gulf of Mexico and the Gulf Stream in the North Atlantic Ocean. Currents through the Caribbean

Sea, the Gulf of Mexico and the Florida Straits constitute an important component of the subtropical gyre circulation of the North Atlanta Ocean, which has been pointed out by Fratantoni (2001) and other researchers. The Loop Current originates at the Yucatan Channel and is the formation region of the Florida Current-Gulf Stream system with peak speeds of 1.5~1.8 ms^{-1} near the surface (Carder et al., 1977; Ochoa et al., 2001). It episodically sheds warm-core rings (Cochrane, 1972; Vukovich, 1995; Sturges and Leben, 2000) at intervals of about 3~17 months. These rings' diameters are 200~300 km with swirl speeds in the range of 1.8~2 ms^{-1}, and they propagate westward at approximately 2~5 $km.day^{-1}$ (Cooper et al., 1990).

APPLICATION OF CSF IN HYCOM

Application of CSF in the momentum equation in the ocean surface Ekman layer

For monochromatic deep water waves, there is a mean Lagrangian volume transport produced in their propagation direction, the Stokes drift (Phillips, 1977), which is expressed as

$$\vec{u}_s = \vec{U}_s e^{2kz} \text{ and } \vec{U}_s = c(ak)^2 \cdot \vec{D}, \tag{1}$$

where $\vec{U}_s$ is the Stokes drift at the ocean surface, a is wave amplitude, k is wave-number, c is wave phase speed, z is depth that is zero at the mean sea level and decreasing downward, and $\vec{D}$ is wave propagation direction. The interaction between the planetary vorticity and the Stokes drift yields a force on the Eulerian momentum balance (Hasselmann, 1970), $\vec{f} \times \vec{u}_s$. Hasselmann (1970) illustrated CSF as the divergence of a wave-induced stress $\tau_w = \overline{\tilde{v}\tilde{w}}$, where $\tilde{v}$ and $\tilde{w}$ are along wave crest component and vertical component of the rapidly varying wave orbital velocity, respectively, which is given by

$$-\rho_w \frac{\partial}{\partial z}\overline{\tilde{v}\tilde{w}} = -\rho_w \mid \vec{f} \times \vec{u}_s \mid. \tag{2}$$

In the classical Ekman layer model, the momentum equation describing the non-steady-state, ageostrophic current in the surface layer is (Wu and Liu, 2008)

$$\frac{\partial \vec{U}}{\partial t} + \vec{f} \times \vec{U} = \frac{\partial}{\partial z}(A_z \frac{\partial \vec{U}}{\partial z}), \tag{3}$$

where $\vec{U}$ is the horizontal current, and A_z is the vertical momentum diffusivity. The corresponding boundary

condition for Equation (3) is

$$\begin{cases} \rho_w A_z \dfrac{\partial \vec{U}}{\partial z} = \vec{\tau}_0 & z = 0 \\ \vec{U} \to 0 & z \to -\infty \end{cases}, \tag{4}$$

in which $\vec{\tau}_0$ is the sea surface wind stress. Introducing the wave-induced stress in the vertical turbulent diffuse term, Equation (3) can be rewritten as

$$\frac{\partial \vec{U}}{\partial t} + \vec{f} \times \vec{U} = \frac{\partial}{\partial z}(\vec{\tau}_* + \vec{\tau}_w), \tag{5}$$

where $\vec{\tau}_* = A_z \dfrac{\partial \vec{U}}{\partial z}$ is turbulent stress, and $\vec{\tau}_w = \overline{\tilde{v}\tilde{w}}$ is wave-induced stress. Incorporating Equation (2) into (5) obtains

$$\frac{\partial \vec{U}}{\partial t} + \vec{f} \times \vec{U} = \frac{\partial}{\partial z}(A_z \frac{\partial \vec{U}}{\partial z}) - \vec{f} \times \vec{u}_s. \tag{6}$$

Equation (6) is consistent with Polton et al.'s (2005) statement, that when the momentum equations are averaged over the wave periods, CSF appears as an extra term in the mean horizontal momentum equations that govern the ageostrophic motions. In Equation (6), the Coriolis force-like CSF is a large-scale wave-induced forcing contributing to the vertical turbulent diffuse term.

Application of CSF in the HYCOM momentum equation

Integration of Equation (2) gives

$$\vec{\tau}_w = -\rho \vec{f} \times \vec{T}_s, \tag{7}$$

$$\vec{T}_s = \int_{-\infty}^0 \vec{u}_s dz = c(ak)^2 \delta_s \cdot \vec{D} = \pi \frac{a^2}{T} \cdot \vec{D} \tag{8}$$

where $\vec{\tau}_w$ is the depth-integrated CSF through the whole Stokes depth δ_s, ρ the water density, $\vec{T}_s$ the depth-integrated wave-induced transport, and T the wave period. The Stokes drift $\vec{u}_s$ and CSF $\vec{f} \times \vec{u}_s$ penetrate to a certain depth from the ocean surface, named Stokes depth scale ($\delta_s = 1/2k$). Typically, the Stokes depth is about 5 m in the open ocean and is much shallower than wind-driven Ekman layer depth (Polton et al., 2005).

Polton et al. (2005), and Wu and Liu (2008) extended

the analytical solutions to the standard Ekman layer model that include CSF, and found that CSF changes the structure of the current profile within the Ekman layer. So, it is reasonable to assume that CSF is confined to the upper ocean ML. Here, the depth-integrated CSF based on the theory of Polton et al. (2005) is added to the momentum Equation of HYCOM (Bleck, 2002) as a boundary condition to examine the effects of Stokes drift on ocean surface circulation. As a boundary condition, CSF does not always enhance the momentum input, but also decreases the momentum input when the wind and CSF are in opposite direction.

In this study, we mainly focus on the ocean surface ML. The mixing strategy used here is the K-Profile Parameterization (Large et al., 1994, 1997). The depth-integrated CSF is also applied to the KPP mixing sub-model as a surface stress (equivalent wind stress) in addition to the traditional one depends solely on the wind. In order to reflect the effects of CSF clearly, here we use the default values for all the tuneable constants in KPP model. Incorporating CSF into the momentum equation of HYCOM in (x, y, s) coordinates (where s is an unspecified vertical coordinate) produces,

$$\frac{\partial \vec{V}}{\partial t_s} + \nabla_s \frac{\vec{V}^2}{2} + (\varsigma + f) \times \vec{V} + (s\frac{\partial p}{\partial s})\frac{\partial \vec{V}}{\partial p} + \nabla_s M - p\nabla_s \alpha = -g\frac{\partial \tau_*}{\partial p} + (\frac{\partial p}{\partial s})^{-1}\nabla_s \cdot (v\frac{\partial p}{\partial s}\nabla_s \vec{V})$$
(9)

where $\vec{V} = (u, v)$ is the horizontal current velocity vector, p pressure, $\alpha = 1/\rho$ the potential specific volume, ς the relative vorticity, $M = gz + p\alpha$ the Montgomety potential, $gz = \phi$ the geopotential, f the Coriolis parameter vector, v the eddy viscosity/diffusivity coefficient, and τ_* the shear stress vector induced by the combination of wind stress, bottom drag and the depth-integrated CSF. Wind stress data in use are all from ECMWF reanalysis. $s\partial p/\partial s$ Represents the vertical mass flux across an s surface. CSF influences the horizontal currents by changing both the shear stress and the eddy viscosity/diffusivity coefficient calculated in the KPP sub-model. The function of CSF in the KPP sub-model and the momentum equation is reflected by changing the effective boundary conditions.

Effects of CSF on the thickness of ocean surface boundary layer (BL) and ML

In the KPP mixing sub-model of HYCOM, the ocean surface Boundary Layer Depth (BLD) h_b is based on the bulk Richardson number, Ri_b, that in the following form

$$Ri_b = \frac{(B_r - B)d}{(\overline{V}_r - \overline{V})^2 + V_t^2},$$
(10)

$$V_t^2 = \frac{C_s(-\beta_T)^{1/2}}{Ri_c \kappa^2}(c_s \varepsilon)^{-1/2} dN\omega_s,$$
(11)

$$\omega_S = \kappa(a_S u_*^3 + c_S \kappa\sigma\omega_*^3)^{1/3} \rightarrow \kappa(c_S \kappa\sigma)^{1/3}\omega_* \quad \sigma < \varepsilon,$$
(12a)

$$\omega_S = \kappa(a_S u_*^3 + c_S \kappa\varepsilon\omega_*^3)^{1/3} \rightarrow \kappa(c_S \kappa\varepsilon)^{1/3}\omega_*$$
$$\varepsilon \le \sigma < 1,$$
(12b)

where B is buoyancy, d is depth, the subscript r denotes reference values, and the two terms in the denominator represent the influence of resolved vertical shear and unresolved turbulent velocity shear, respectively. Reference values are averaged over the depth range εd, where $\varepsilon = 0.1$. At depth of $d = h_b$, the reference depth εh_b represents the thickness of the surface layer where the Monin-Obukhov similarity theory applies. The unresolved turbulent velocity shear is expressed as Equation (11), where C_S is a constant between 1 and 2, β_T is the ratio of entrainment buoyancy flux to surface buoyancy flux, $\kappa = 0.4$ is the von Karman constant, and ω_S is the salinity/scalar turbulent velocity scale, which is estimated from Equation (12). In Equation (12), a_S and c_S are constants, $\omega_* = (-B_f/h)^{1/3}$ is the convective velocity scale with B_f representing the surface buoyancy flux, σ equals to d/h_b, and the friction velocity u_* is from the relation $u_*^2 = |\tau|/\rho$, where τ includes surface wind stress (ECMWF Reanalysis) and CSF. Terms on the right side of the arrows in both Equations (12a) and (12b) are the convective limits. BLD is the depth range over which the turbulent boundary layer eddies can penetrate before becoming stable relative to the local buoyancy and velocity, and is often characterized by very small vertical property gradients over large portions of its central region. BLD is estimated as the minimum depth at which Ri_b exceeds the critical Richardson number $Ri_c = 0.3$. As mentioned above, h_b is based on Ri_b, Ri_b is a function of u_*, and u_* is influenced by CSF, thus BLD h_b can be influenced by CSF.

In the KPP mixing strategy, MLD is estimated diagnostically depending on a temperature jump, e.g. 0.3°C. The base of the ML is set to an interpolated depth where the density jump is equivalent to the temperature jump. Usually, BLD and MLD are similar, since KPP mixes strongly down to BLD, so density should be relatively homogeneous throughout the whole layer. BLD

Table 1. The model settings of the 6 experiments.

Experiments		Exp. 1	Exp. 2	Exp.3	Exp. 4	Exp. 5	Exp.6
Domain		Global	Global	SCS	SCS	WNA	WNA
Resolution	Latitude	$2.5° \times \cos\varphi$	$2.5° \times \cos\varphi$	$1/12° \times \cos\varphi$	$1/12° \times \cos\varphi$	$1/6°$	$1/6°$
	Longitude	$2.5°$	$2.5°$	$1/12°$	$1/12°$	$1/6°$	$1/6°$
Coriolis-Stokes		Yes	No	Yes	No	Yes	No

and MLD are determined by different criteria, the former is by buoyancy and the latter temperature. Actually, buoyancy and temperature can be linked through density. Thus, the effects of CSF on MLD are similar to those on BLD.

Effects of CSF on SST

The temperature conservation equation in HYCOM is

$$\frac{\partial}{\partial t_s}(\frac{\partial p}{\partial s}T) + \nabla_s \cdot (\vec{V}\frac{\partial p}{\partial s}T) + \frac{\partial}{\partial s}(\dot{s}\frac{\partial p}{\partial s}T) = \nabla_s \cdot (\upsilon\frac{\partial p}{\partial s}\nabla_s T) + S_T$$

(13)

where T is temperature, υ the eddy viscosity/diffusivity coefficient, S_T the diabatic source terms including diapycnal mixing. As presented under application of CSF in the HYCOM momentum equation, CSF impacts horizontal current velocity $\vec{V}$ through the momentum equation. Since $\vec{V}$ plays its part in the second term of temperature conservation equation Equation (13), CSF also influences SST. Additionally, CSF intensifies/weakens turbulent mixing in the upper ocean by modifying the diffusivity coefficient as an effective top boundary condition for the KPP sub-model. Thus, it also leads to the change of SST. The effects of CSF on salinity are similar to that on temperature, but they are beyond the scope of this study.

MODEL SETTINGS AND EXPERIMENTS

Three sets of experiments (Table 1) with different horizontal resolutions and in different regions are designed for the current study. HYCOM and WW3 are chosen to conduct those numerical experiments. Considering the length limit, introductions, such as numerical technique, about HYCOM and WW3 please refer to the User's Menu.

Global experiments

Two experiments, Experiments 1 and 2 modeled with and without CSF, respectively, are conducted for the global ocean. The calculation domain for HYCOM is from 64.43911°S to 64.43911°N with a resolution of $2.5° \times \cos\varphi$ in latitude, where φ is the corresponding latitude, and 180°W to 180°E with a resolution of 2.5° in longitude, with an array size of 144×69 horizontal grid points. 26 hybrid layers are used in the vertical. HYCOM is initialized by the Polar Science Center Hydrographic Climatology (PHC) 3.0. This monthly climatology is also used for lateral boundary nudging and relaxation of salinity and temperature on the ocean surface. The model is spun up for 5 years forced by ERA15 ECMWF reanalysis monthly climatology. The forcing variables are 10 m winds, ocean surface air temperature, precipitation, radiation heat flux, short-wave radiation, and water vapor mixing ratio.

Then, 24-hourly ECMWF ERA40 wind anomalies are added to ECMWF ERA15 climatology to produce the 2001 run. In addition, the CSF is added in Experiment 1. WW3 is configured on a grid from 90°S to 90°N with a resolution of 2.5° and 180°W to 180°E with a resolution of 2.5°, which gives a total of 144×73 horizontal grid points. The first frequency is 0.0418 Hz, the frequency increment factor is 1.1, the number of frequencies is 30, and the directional resolution is 15°. Minimum source term time step is 600 s. Time interval of wind input is 86400 s. Input winds are from ECMWF ERA40 re-analysis data sets.

SCS experiments

Another two experiments, Experiments 3 and 4 run with and without CSF, are conducted for SCS region. The model domain for HYCOM is from 3.24696°S to 22.705°N with a resolution of $1/12° \times \cos\varphi$ degree in latitude and 102°E to 120.9924°E with a resolution of 1/12° in longitude, and a total grid size of 229×320. The number of the vertical hybrid layers is 26. For WW3, a horizontal grid size of 39×55 is configured for a domain from 4°S to 23°N with a resolution of 0.5° in latitude and 102°E to 121°E in longitude with a resolution of 0.5°. The boundaries of the calculation domain are closed. The Taiwan Strait, Luzon Strait, Gaspar Strait, Karimata Strait and Strait of Malacca are treated as closed boundary condition, which means no water pass through those boundaries and only the salinity and temperature are relaxed in the buffer zones. The rest of the settings are the same as that of the global run.

WNA experiments

Experiments 5 and 6 are simulations with and without the effect of CSF in WNA region. The WNA domain has a grid size of 181×205 with a horizontal resolution of 1/6°, from 263°E to 293°E in longitude and 8°N to 42°N in latitude, and 26 vertical layers. It is nested in the North Atlantic 2.00 (horizontal resolution is 2°) domain which provides boundary conditions to the finer WNA domain. The WW3 is configured for the same domain, but with a different horizontal resolution of 0.5°. The other settings are the same as that of the global case.
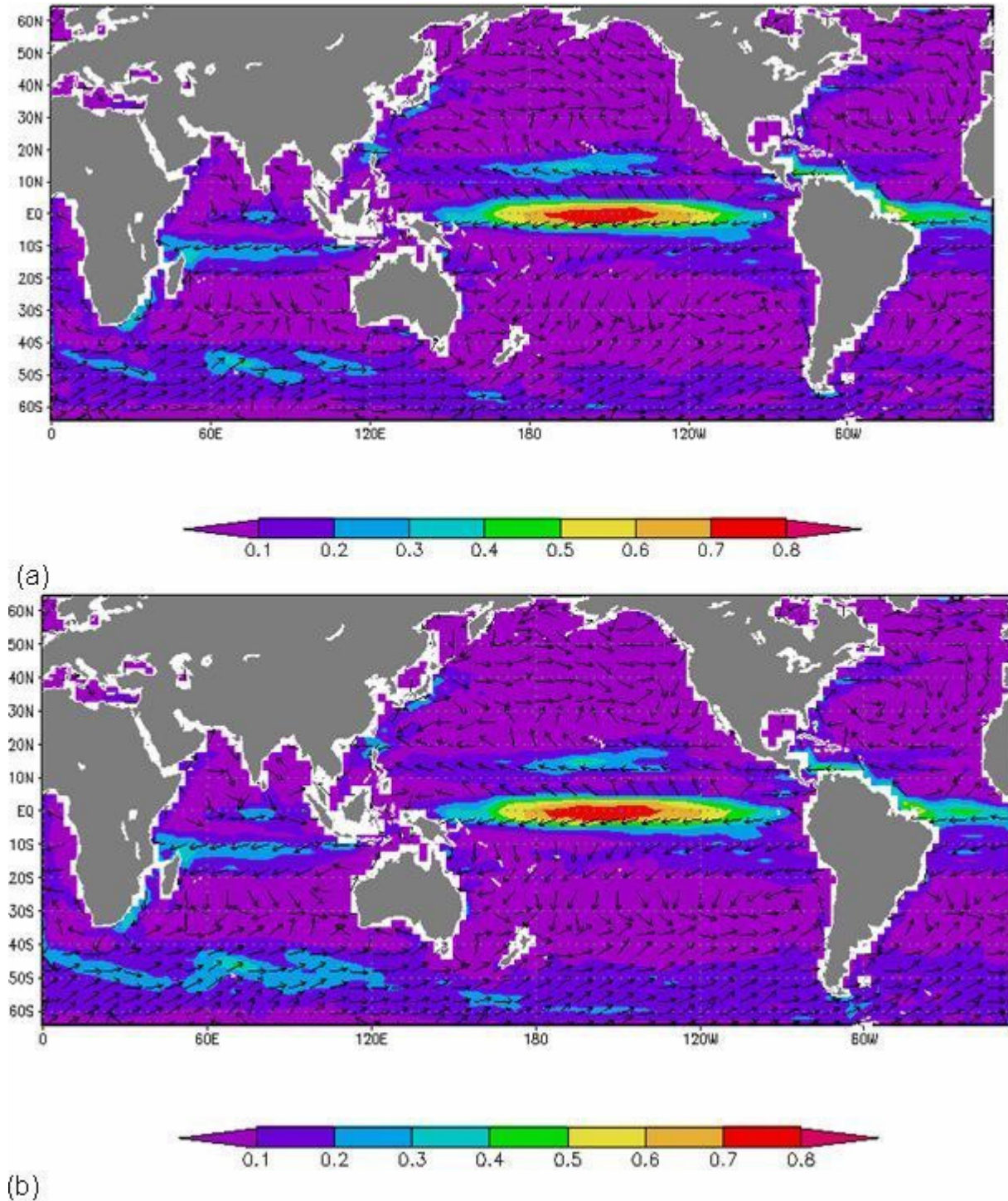
Figure 1. a) Annual-mean mixed-layer current field of 2001 from Exp. 2; b) Annual-mean mixed layer current field of 2001 from Exp. 1 (ms^{-1}).

MODELING RESULTS

Global case

Figures 1a and b show the details of the global ML

current fields from Experiments 1 and 2, respectively. The South Equatorial Current (SEC), North Equatorial Current (NEC), Equatorial Current (EC), and Western Boundary Current (WBC) such as the Kuroshio Current and the Gulf Stream, are clearly shown. The resolution used in

the global case is 2.5° which is not fine enough to resolve WBC, so WBC is not as noticeable as EC in this situation. By comparing Figure 1a with 1b, we find that the two figures have the same pattern. It indicates that although the wave-induced CSF exerts an influence, as illustrated in Figure 2c, in the upper ocean ML, especially over the Westerly region, it can not fundamentally change the structures of the current field. Figures 1 and 2a show that, both the global ocean surface circulation and waves are basically subject to the wind field (as a common sense, the wind field is not shown).

Figures 2a and b present the annual-mean depth-integrated Stokes transport $\vec{T}_s$ which is calculated by the wave variables from the WW3 simulation and the ECMWF reanalysis, respectively. The general patterns of $\vec{T}_s$ in both cases agree well over the global ocean, and the directions of $\vec{T}_s$ are quite similar over the Westerly regions. This indicates that the wave variables modeled by WW3 are reasonable. The ML depth-integrated current transport is expressed as $\vec{T}_c = \int_{-d}^{0} \vec{V}_z dz$, where $\vec{V}_z$ is the current velocity and d refers to the MLD. CSF-induced changes in ML depth-integrated current transport $\Delta \vec{T}_c$ are presented in Figure 2c, with most of the values range from 0 to 3 m^2s^{-1}. Almost all the large values are located over the high-latitude Westerly wind belt with a maximum of 13 m^2s^{-1}, where relatively strong winds force large waves. Note that the values of Stokes transport $\vec{T}_s$, from both WW3 simulation and ECMWF reanalysis, are in the ranges of about 0 to 2.2 m^2s^{-1}. It is safe to assume that most of the values of both $\vec{T}_s$ and $\Delta \vec{T}_c$ are in the similar order. Figure 2d gives the wave-induced percentage changes in $\vec{T}_c$ (defined as $\Delta \vec{T}_c / \vec{T}_c$) which reveals the significant effect of CSF on the upper ocean currents. Changes in the tropical region and the western boundary current regions are relatively small, about 10%. Over the mid-latitude region, especially those under the Westerlies, the changes are more than 30%; with largest value reaches 90%, due to the strong wind waves acting on the relatively weak currents there. In the ocean model, the ocean surface Ekman layer is usually characterized as an ocean surface BL. Since BL and ML have the same depth scale, the wave-induced percentage changes in $\vec{T}_c$ can be considered as a gauge of how important the wave-induced $\Delta \vec{T}_c$ is, relative to Ekman transport. From Figures 2a, b and c, it is interesting to note that, there are large differences between the directions of $\Delta \vec{T}_c$ and $\vec{T}_s$, except for the Southern Hemisphere Westerlies (especially in the Pacific) where comparatively good agreement can be found.

According to Equation (3), the direction of CSF is perpendicular to that of the waves, so the expected direction of $\Delta \vec{T}_c$ will also be normal to $\vec{T}_s$. As shown in Figures 2a and c, the direction of $\Delta \vec{T}_c$ is similar to that of $\vec{T}_s$, where strong winds directly force large waves; in the swell-dominant tropical region, the direction of $\Delta \vec{T}_c$ appears to be normal to that of the waves or $\vec{T}_s$ since swell propagates from remote areas (Deng et al., 2007,2009), while in some other places, the direction of $\Delta \vec{T}_c$ and $\vec{T}_s$ are almost opposite, which can be explained as, that the wave-induced Stokes transport $\vec{T}_s$ is compensated by the CSF.

Theoretically, the direction of $\Delta \vec{T}_c$ over the southern and northern Westerly regions should be symmetrical since the CSF is equator-ward for both of the two regions where wind direction is eastward. However, the actual situation of the northern Westerly region is out of our expectation. Possible reason for that could be the different topography and different wind wave intensity or other unclear influence over these two regions. This phenomenon is worthy of further investigation. In the global ocean surface ML, the CSF-caused changes in MLD (Δthi) are in the range of -15 to 80 m (Figure 3a). There is an obvious enhancement of MLD in the southern Westerlies where the value of Δthi is 24 m on average. It is due to the fact that the strong wind waves prevail in this region and CSF intensifies the mixing in the upper ocean by interacting with the currents. In most regions of the northern hemisphere, the values of Δthi are decreased, because the wave-induced CSF weakens the net forcing (a combination of wind stress, CSF and so on) in these places. For example, if the wave-induced CSF and wind stress are in the same (different) direction, the net forcing will be increased (decreased).

As for the influences of CSF on ocean surface temperature over the global ocean (Figure 3b), the Δtem value varies from -0.8 to 0.8℃; the maximum value, as large as 0.8℃, appears along the very close eastern boundary of the southern Pacific where both $\Delta \vec{T}_c$ and $\vec{T}_s$ originating from the cold southern Westerly region (carrying cold water). Deng et al. (2007) presented that, the total wave-induced equator ward Stokes transport from Westerlies is 3.672 Sv on average over the swell-prevailed Eastern Pacific region, and $\vec{T}_s$ over the eastern boundary of the Southern Pacific area is noticeable. The majority of the positive (negative) Δthi values correspond to the negative (positive) Δtem values, since mixing intensified (weakened) by CSF decreases (increases) ocean surface temperature by entraining
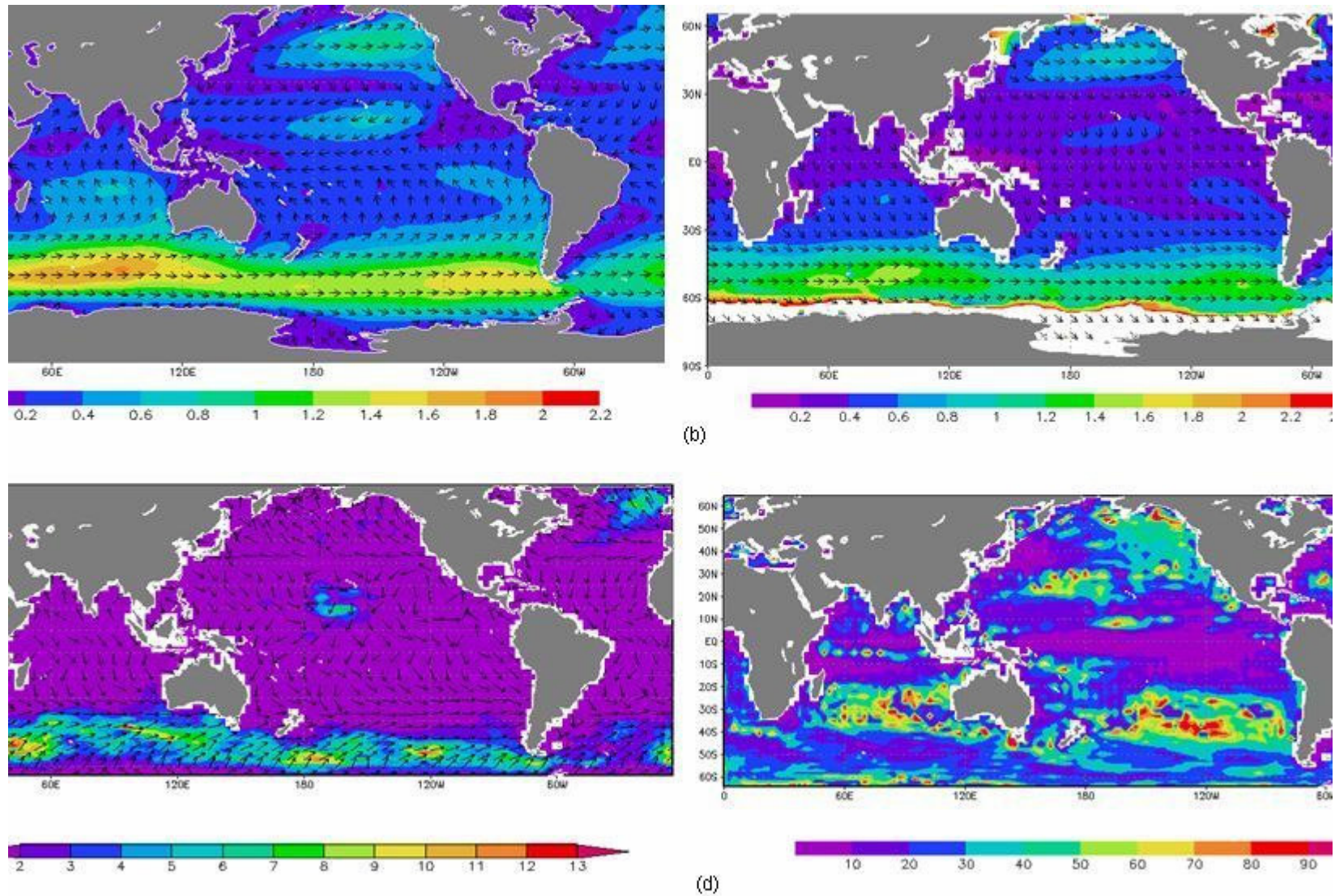
Figure 2. a) Annual-mean depth-integrated wave-induced Stokes transport, $\vec{T}_s$, of 2001 (simulated by WW3 model, m²s⁻¹), b) Annual-mean depth-integrated wave-induced Stokes transport, $\vec{T}_s$, of 2001 (calculated by ECMWF reanalysis wave variables, m²s⁻¹), c) Annual-mean changes (results of Exp. 1 minus that of Exp. 2) in depth-integrated current transport through the mixed layer, $\Delta\vec{T}_c$, of 2001 (m²s⁻¹), and d) percentage change of $\vec{T}_c$ ($\Delta\vec{T}_c/\vec{T}_c$). (Color indicates the magnitude and vector presents the direction).
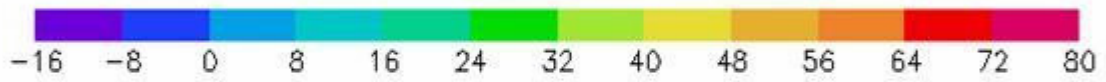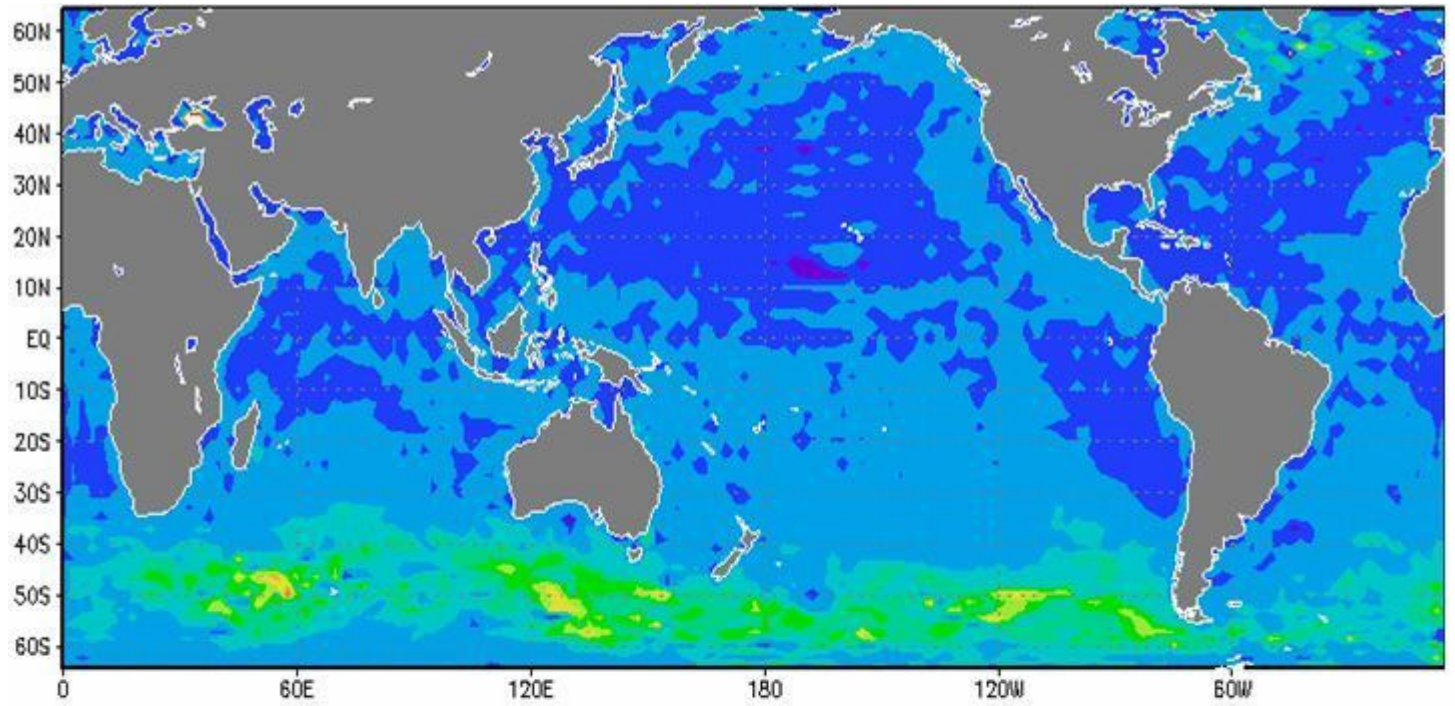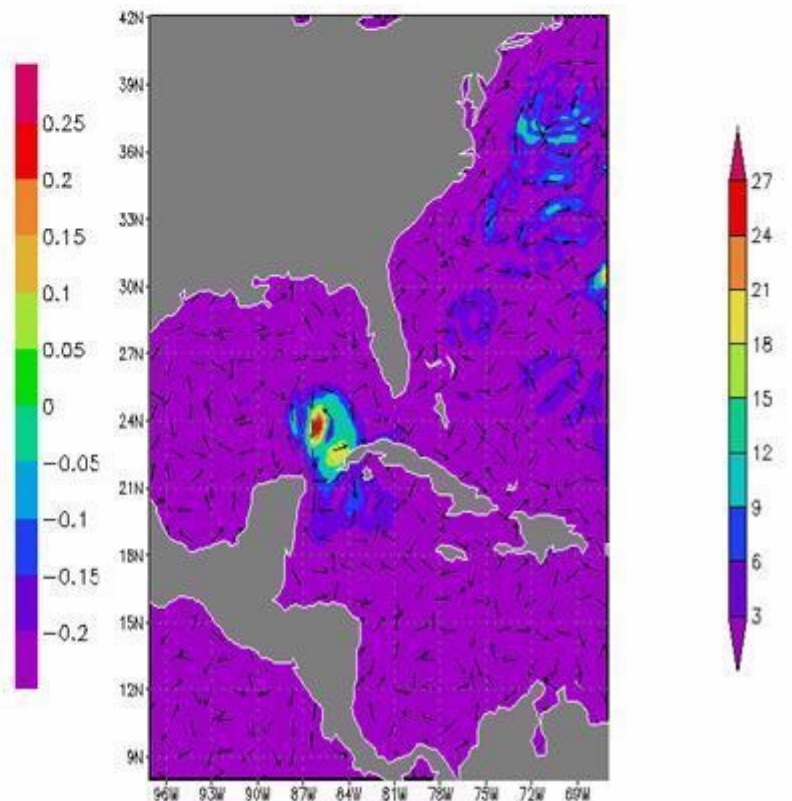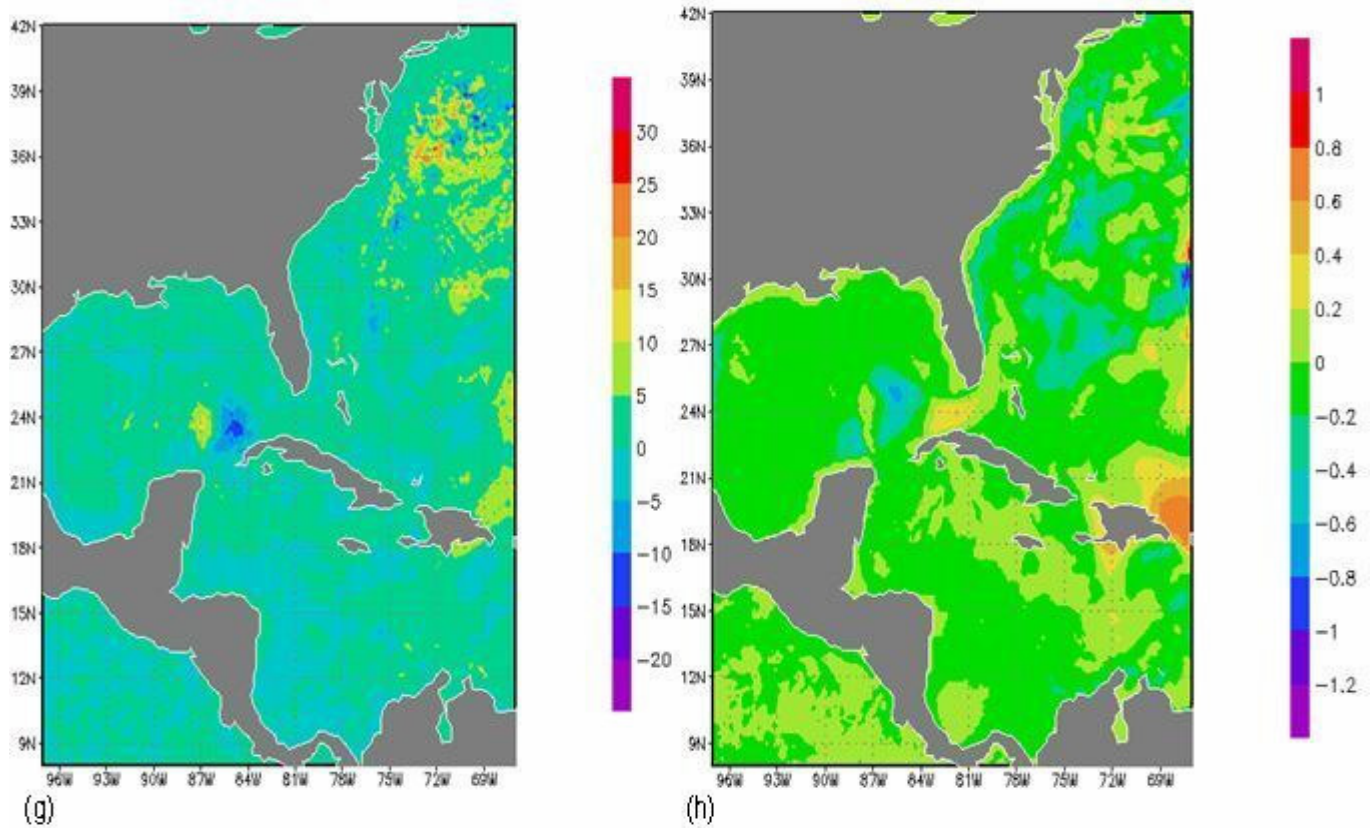
(a)
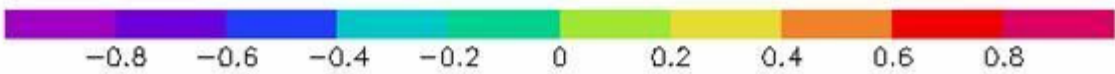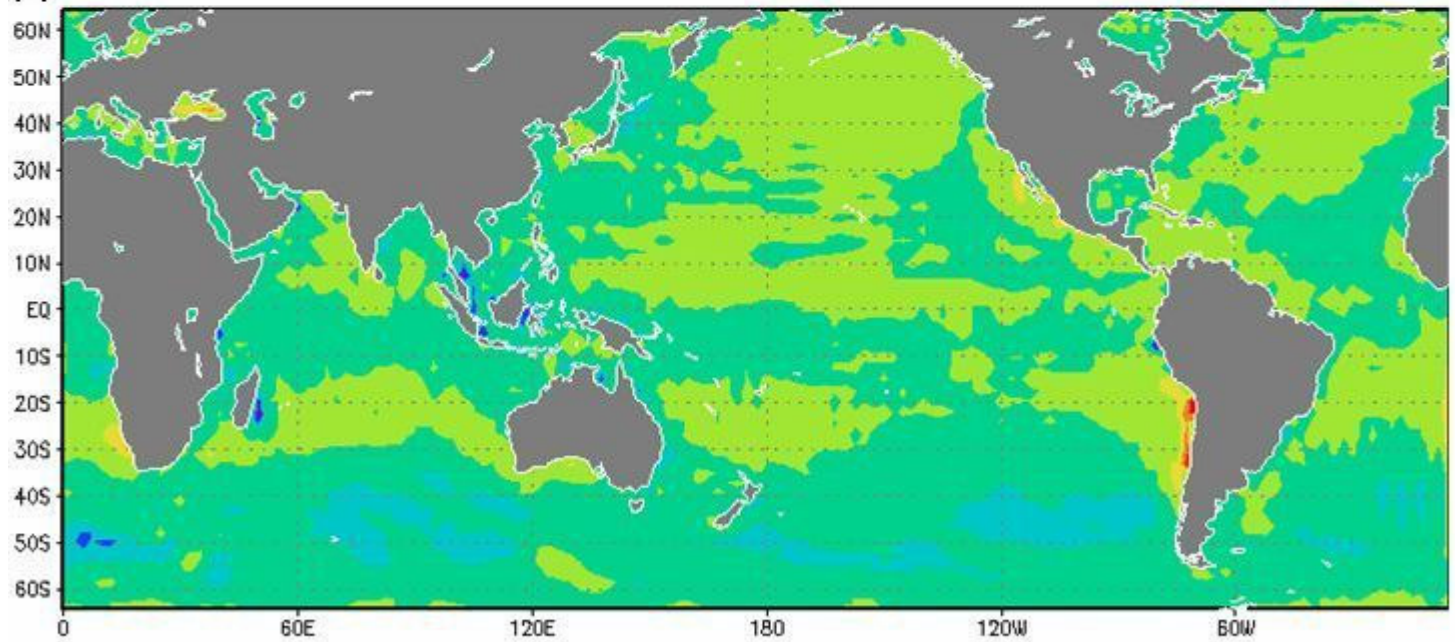
(b)
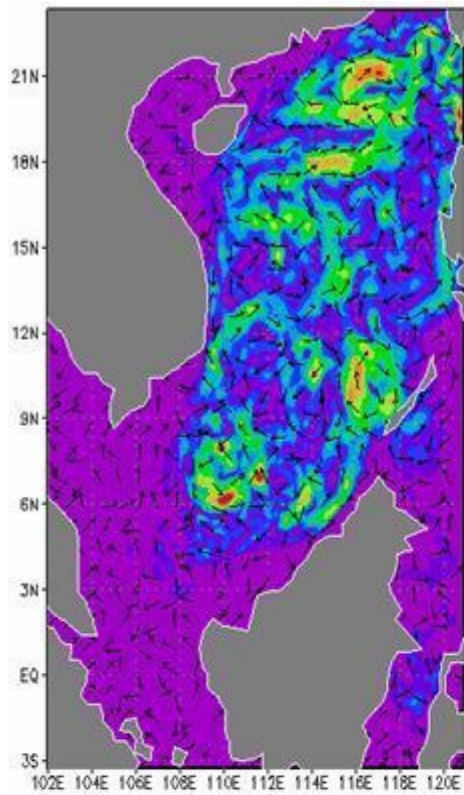
(c)
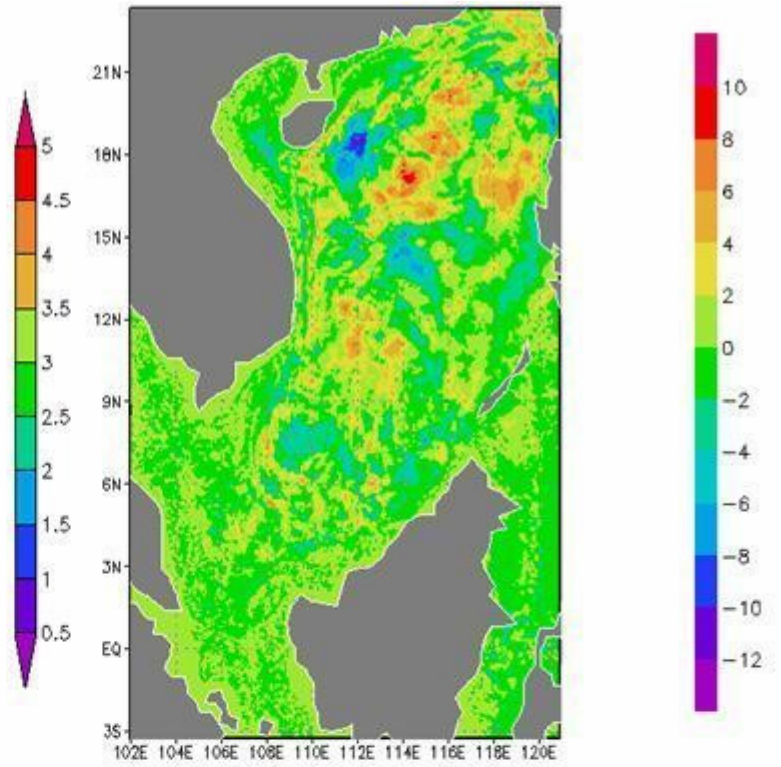
(d)
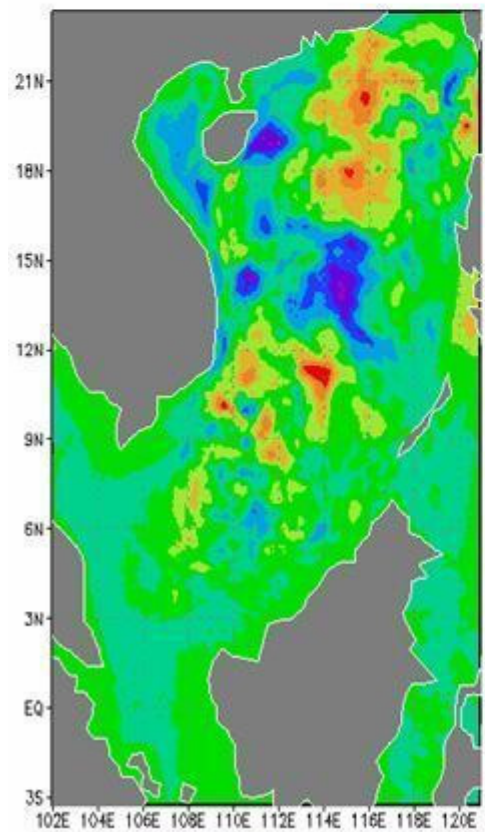
(e)

(f)

Figure 3. a) Annual-mean changes in mixed layer depth , Δthi , of 2001in the global ocean (results of Exp. 1 minus that of Exp. 2, *m*); b) Annual-mean changes in mixed layer temperature, Δtem , of 2001 in global ocean (results of Exp. 1 minus that of Exp. 2, m); c) Annual-mean changes in mixed layer depth-integrated current transport, $\Delta \vec{T}_c$, of 2001 in SCS (results of Exp. 3 minus that of Exp. 4, m²s⁻¹); d) Annual-mean changes in mixed layer depth, Δthi , of 2001 in SCS (results of Exp. 3 minus that of Exp. 4, *m*); e) Annual-mean changes in mixed layer temperature, Δtem , of 2001 in SCS (results of Exp. 3 minus that of Exp. 4, ℃); f) Annual -mean changes in mixed layer depth-integrated current transport, $\Delta \vec{T}_c$, of 2001 in WNA (results of Exp. 5 minus that of Exp. 6, m²s⁻¹); g) Annual-mean changes in mixed layer depth, Δthi , of 2001 in WNA (results of Exp. 5 minus that of Exp. 6, *m*); and h) Annual-mean changes in mixed layer temperature, Δtem , of 2001 in WNA (results of Exp. 5 minus that of Exp.6, ℃). (Color indicates the magnitude and vector presents the direction).

more (less) cold water into the ML.

SCS Case

Figures 3c to e present the distribution of annual-mean $\Delta \vec{T}_c$, Δthi , and Δtem in SCS, respectively. The magnitude of annual-mean $\Delta \vec{T}_c$ varies from 0 to 5 m²s⁻¹ with large values located in regions, where the two main gyres emerge in both winter and summer. The influences of wave-induced CSF on $\vec{T}_c$ are apparently more significant in these gyre regions. In other regions, the values of $\Delta \vec{T}_c$ are less than 1 m²s⁻¹. The direction of $\Delta \vec{T}_c$

seems random as annual-mean vectors cannot capture the variations of the impacts of CSF that varies from month to month. The values of annual-mean Δthi are in the range of -10 to 10 m, with large positive values existing to the west of the Luzon Strait where cyclonic gyres exist. The relatively small ML temperature change varying from -0.2 to 0.25℃ compared with the global case, indicates that the horizontal resolution influences the modeling results.

The annual evolution of the ML current field in SCS (Figure 4, only odd months are shown) characterized by two main basin-scale eddies can be found in each month. Figure 5 shows the variability of $\Delta \vec{T}_c$ resulted from CSF for each odd month. Since all the connections that link SCS to the surrounding seas are closed, in the case of
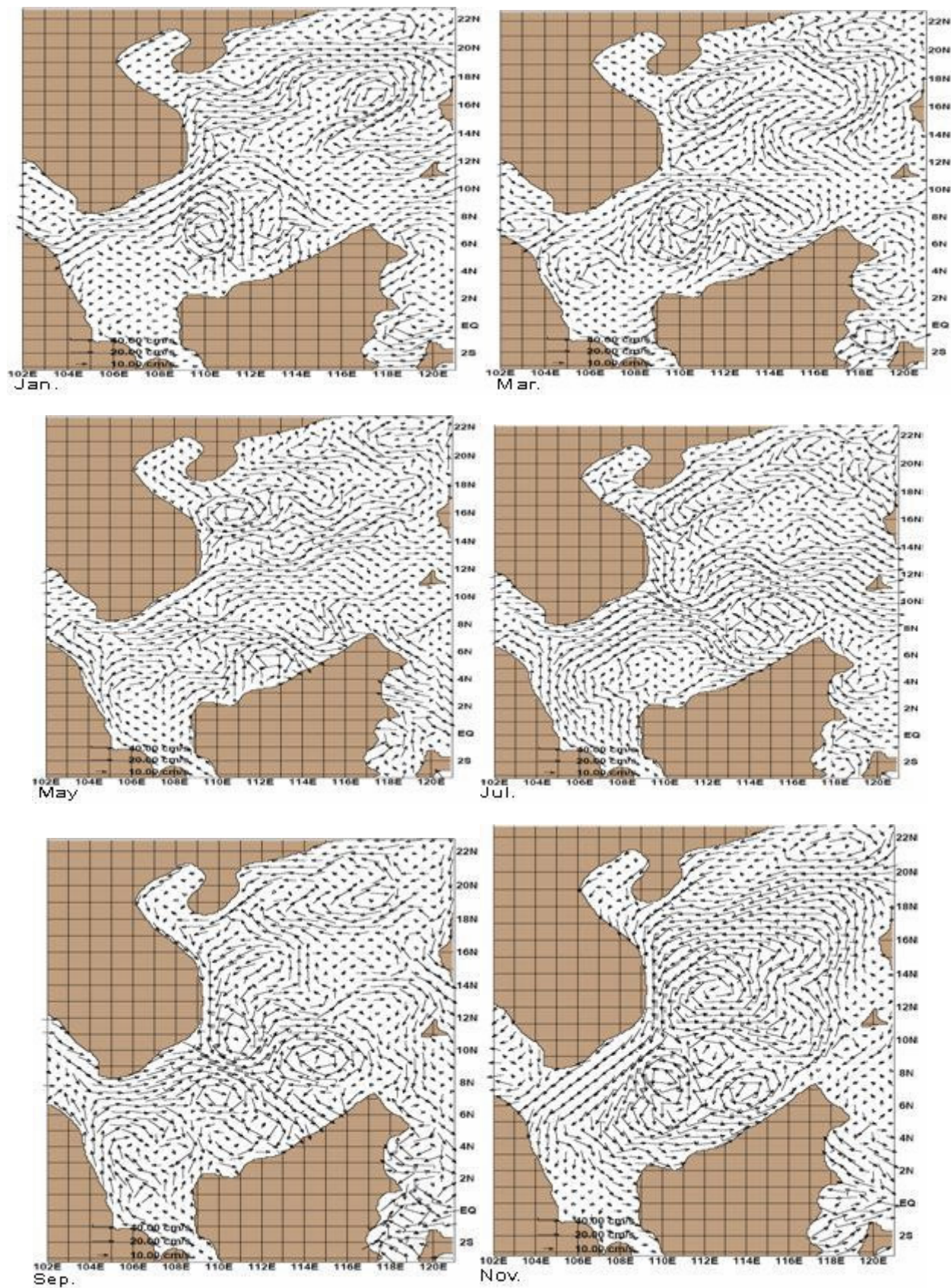
Figure 4. Monthly-mean mixed layer current field in 2001 over SCS (from Exp. 4, $cm \cdot s^{-1}$).
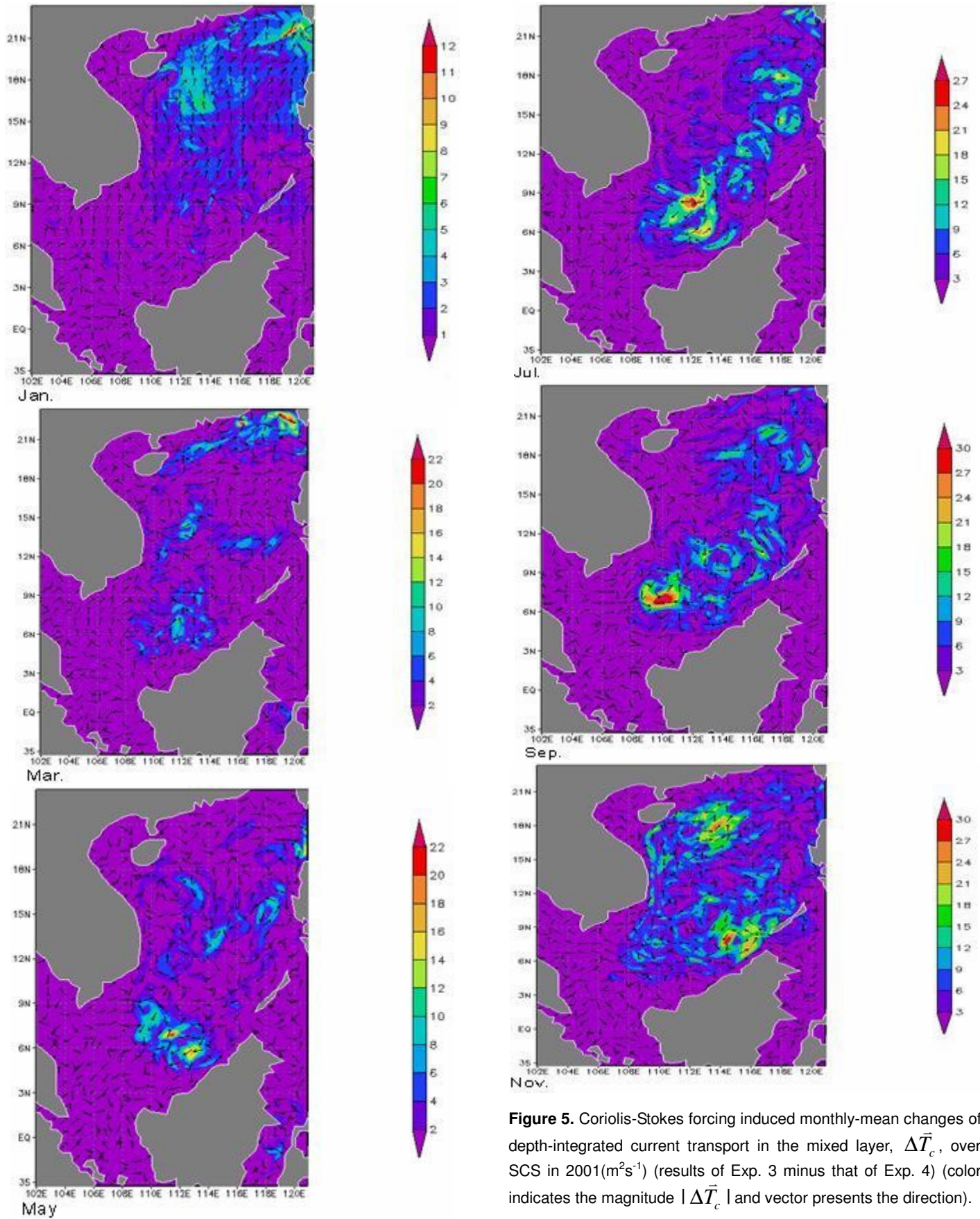
Figure 5. Coriolis-Stokes forcing induced monthly-mean changes of depth-integrated current transport in the mixed layer, $\Delta\vec{T}_c$, over SCS in 2001(m²s⁻¹) (results of Exp. 3 minus that of Exp. 4) (color indicates the magnitude $|\Delta\vec{T}_c|$ and vector presents the direction).

no CSF, our modeled circulation is a result of the interaction of local wind-driven circulation with topography. The upper layer circulation of SCS is mainly driven by the monsoon circulation. Wyrtki (1961) demonstrated that, there is a distinct seasonal cyclonic gyre in winter and a weak cyclonic gyre in the Northern SCS, but an anti-cyclonic gyre in the southern SCS in summer. In terms of the basin-scale gyre, our modeling results are consistent with that of Wyrtki (1961). Qu (1999) showed similar results by an analysis of the distribution of dynamic height. Liu et al. (2008) found that the barotropic sea surface height has a seasonal distribution similar to that of the sea dynamic height. Another important current in SCS, the Vietnam coastal jet, flows southward during winter monsoon season and reverses in summer, which is also in good agreement with the result of Wyrtki (1961). According to Figure 4, during winter monsoon, the southward coastal jet off Vietnam is displayed as a continuation of the southwestward coastal jet over the continental slope south of China, named the Dongsha Current, since it originates near Dongsha Island. In summer, the northward jet off Vietnam turns eastward into the interior of SCS at about 11°N.

Next, comparing $\Delta \vec{T}_c$ in each odd month with the corresponding current field, Figure 5 provides an insight into the influences of CSF on $\Delta \vec{T}_c$. In January, the magnitudes of $\Delta \vec{T}_c$ are generally between 0 and 5 m^2s^{-1}, and the larger values are distributed over the northern SCS; in the north part of SCS, especially west of the Luzon Strait, and the region to the south of the Vietnam coast, the directions of $\Delta \vec{T}_c$ are generally northward and generally normal to that of the currents there. Knowing that the northeasterly winter monsoon winds are prevailing in this season, this phenomenon can be explained, at least theoretically, by the fact that the flow driven by CSF is normal to the quasi-geostrophic gyre currents. In November, the situation is similar to that of January except that the distribution of large $\Delta \vec{T}_c$ values extends through to south SCS. Also, the maximum value of $\Delta \vec{T}_c$ is larger. From the earlier two winter cases, it can be found that large $\Delta \vec{T}_c$ value centers are always located at the cyclonic/anti-cyclonic gyre region which suggests that CSF plays an important role there. However, some large $\Delta \vec{T}_c$ values also appear in other places. In summer months, both May and July, the circulation is depicted by a weak cyclone in the north part of SCS and an anti-cyclonic in the south due to the actions of southwesterly summer monsoon winds. The large $\Delta \vec{T}_c$ value center is developed in the southern SCS, between 5°N and 9°N in latitude and 110°E and 114°E in longitude, where strong eastward currents exist.

No obvious relationship can be found between the current direction and the $\Delta \vec{T}_c$ direction.

WNA Case

For the WNA region, $\Delta \vec{T}_c$, Δthi and Δtem are shown in Figures 3f, g and h, respectively. The majority of $|\Delta \vec{T}_c|$ are less than 6 m^2s^{-1} with a maximum of 27 m^2s^{-1} occurring between Yucatan Channel and Straits of Florida where the Loop Current is located at. It also indicates that, as in the SCS case, the influences of CSF on upper layer current field are stronger in regions with strong quasi-geostrophic currents. The value of annual-mean Δthi generally varies in the range of -20 to 30 m, most of them from -10 to 10 m. Large variability of MLD is found in the Loop Currents region and northern part of Atlantic, where intense currents exist. The annual-mean changes in ML temperature due to CSF are between -1 and 1°C. A great portion of Δtem values fall in the range of -0.4 to 0.4°C. As discussed earlier, mixing intensified (weakened) by CSF decreases (increases) ocean surface temperature by entraining more (less) cold water into the ML leading to the changes in both MLD and temperature.

Monthly-mean ML current fields (including the effects of CSF), for March, June, September and December of 2001, are given in Figure 6, with the western boundary currents (Caribbean Current and Loop Current as well as the Gulf Stream) clearly depicted. In the Gulf of Mexico region, the ring shed off by the Loop Current has a diameter of about 250 km which is consistent with previous model results. We also notice that the core of the ring exists at (89.5°W, 25.5°N) in January and it dissipates at the western boundary of Gulf of Mexico in June. It takes roughly 6 months for the eddy to cross the Gulf of Mexico, corresponding a westward propagation speed of approximately 3 $km \cdot day^{-1}$, which agrees well with the result given by Romanou et al. (2004). Another interesting issue to note is that the Loop Current becomes weaker and weaker while another eddy is developing in the Caribbean Sea south of the Yucatan Channel during the period of June to December.

As mentioned earlier, CSF can influence the upper ocean circulation to a certain degree, but cannot fundamentally change the current pattern. It just serves as a correction to the ocean top boundary condition. The monthly-mean ML $\Delta \vec{T}_c$ in WNA for March, June, September, and December of 2001 are shown in Figure 7. Similar to SCS, the magnitudes of $\Delta \vec{T}_c$ are generally less than 5 m^2s^{-1}. The large ones appear in the area where intense eddy present, such as the Loop Current region and the Gulf Stream region. One possibility is that the dynamic process in the strong eddy/gyre region is
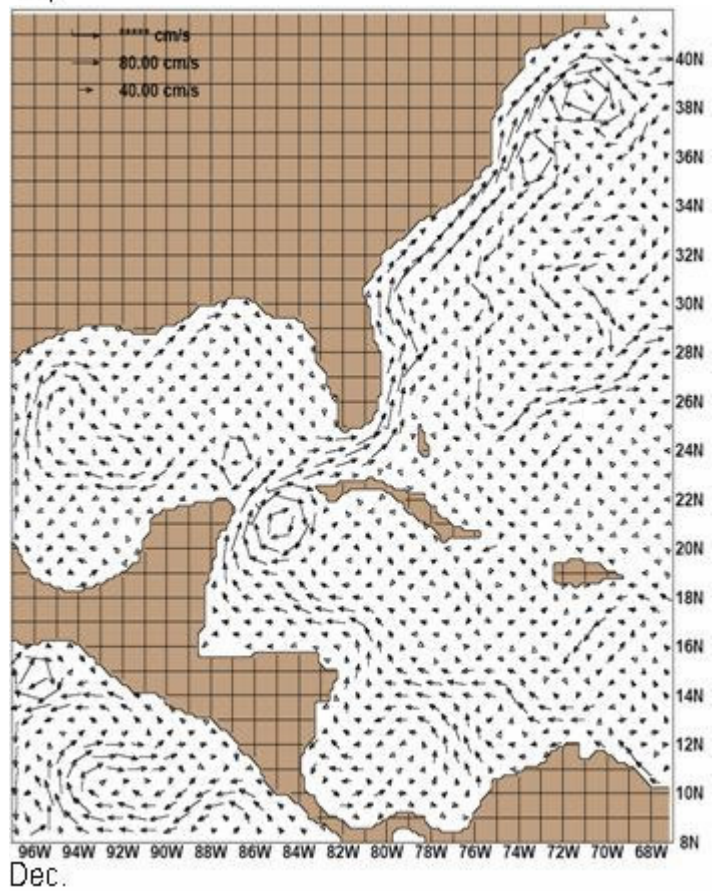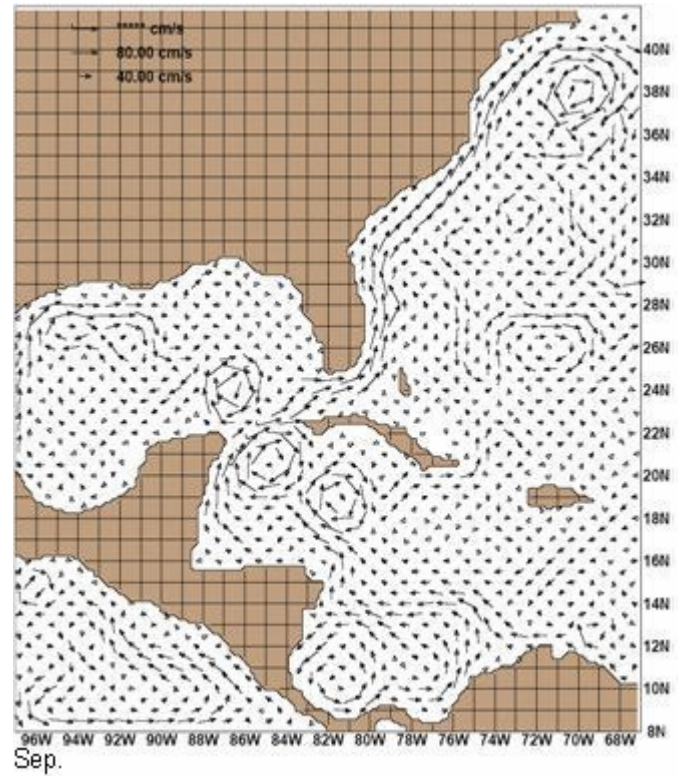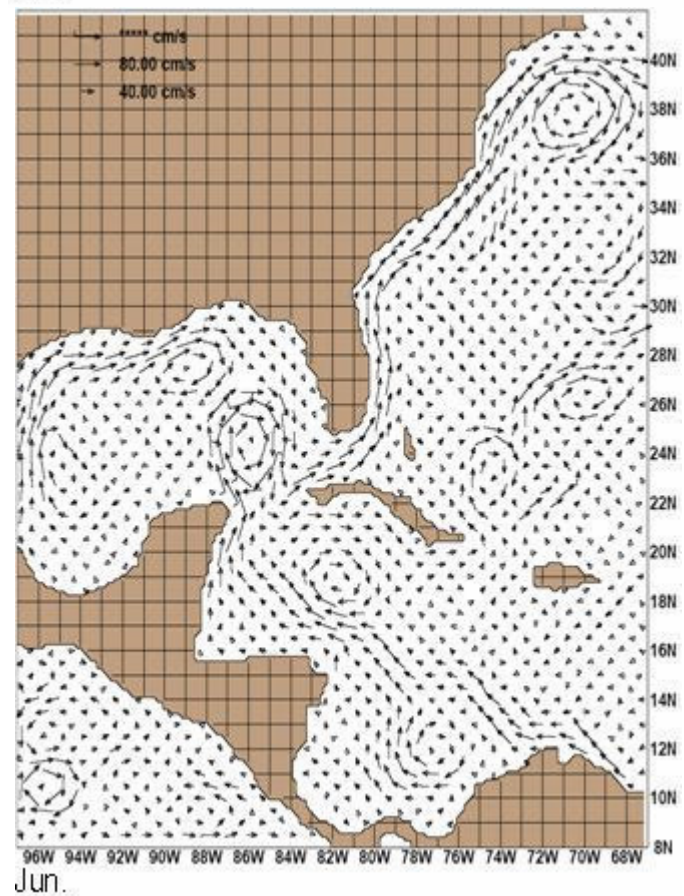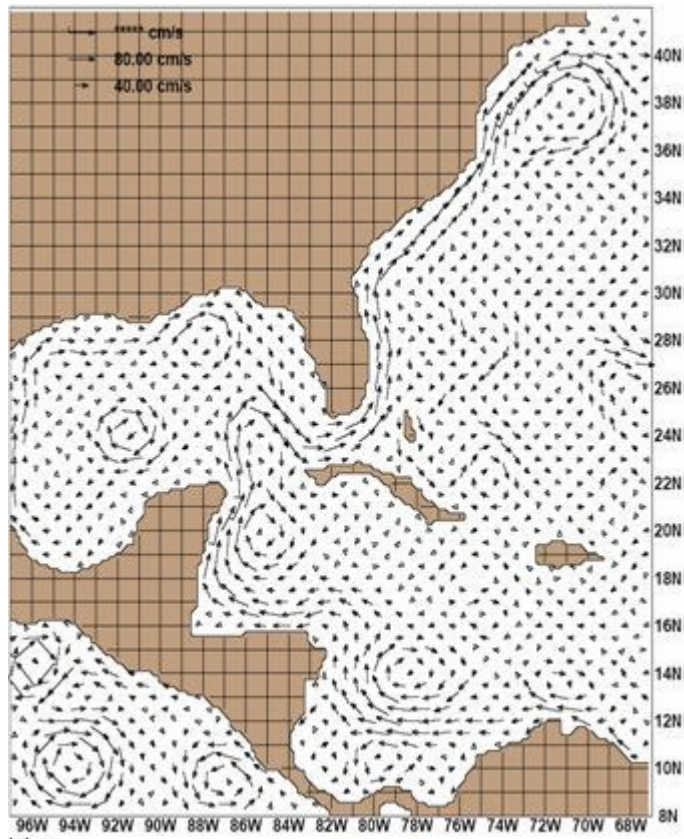
Figure 6. Monthly-mean mixed layer current field in 2001over WNA (from Exp. 5, $cm \cdot s^{-1}$).
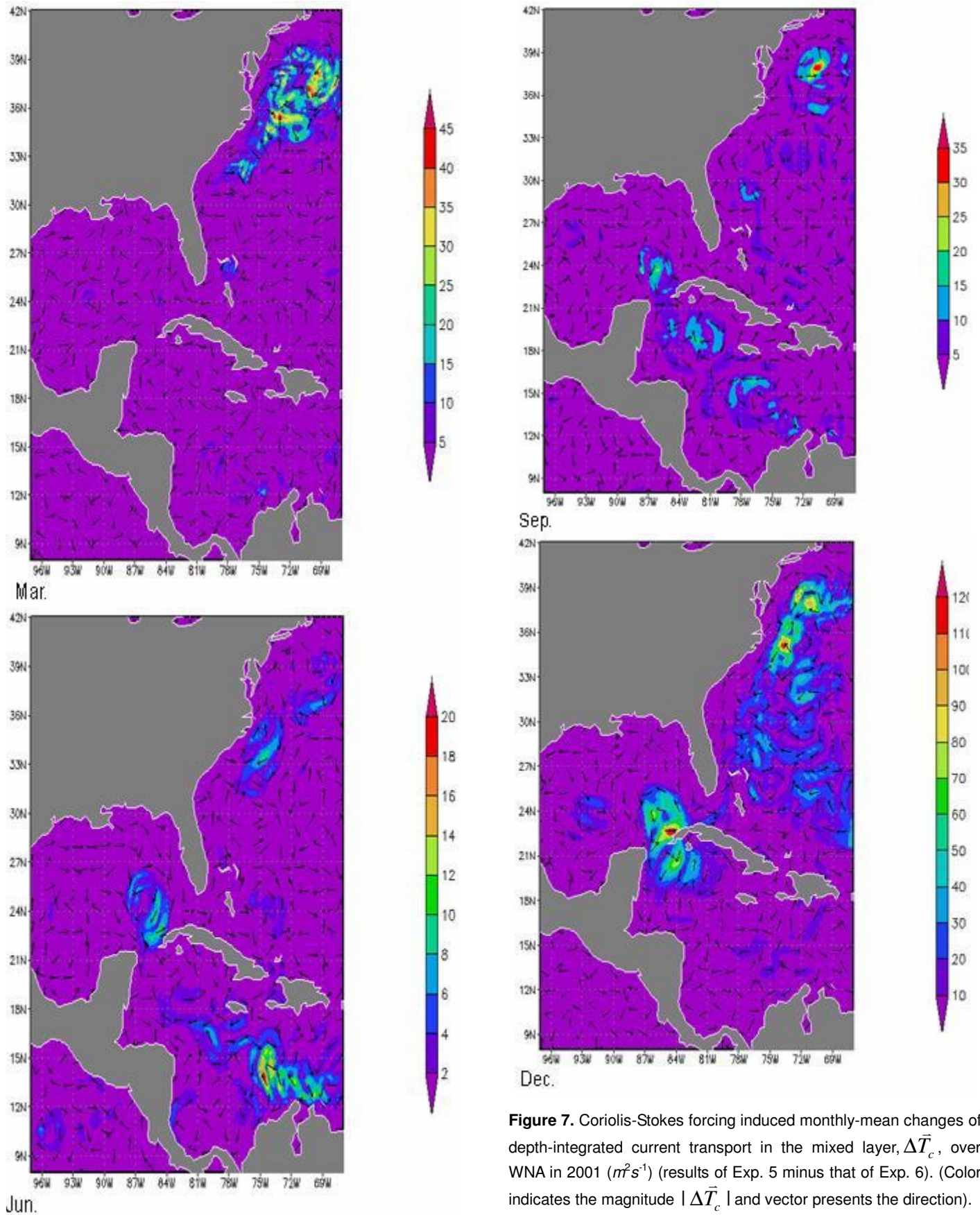
Figure 7. Coriolis-Stokes forcing induced monthly-mean changes of depth-integrated current transport in the mixed layer, $\Delta\vec{T}_c$, over WNA in 2001 (m^2s^{-1}) (results of Exp. 5 minus that of Exp. 6). (Color indicates the magnitude $|\Delta\vec{T}_c|$ and vector presents the direction).

Station: (0N,140W)

Station: (0N,155W)

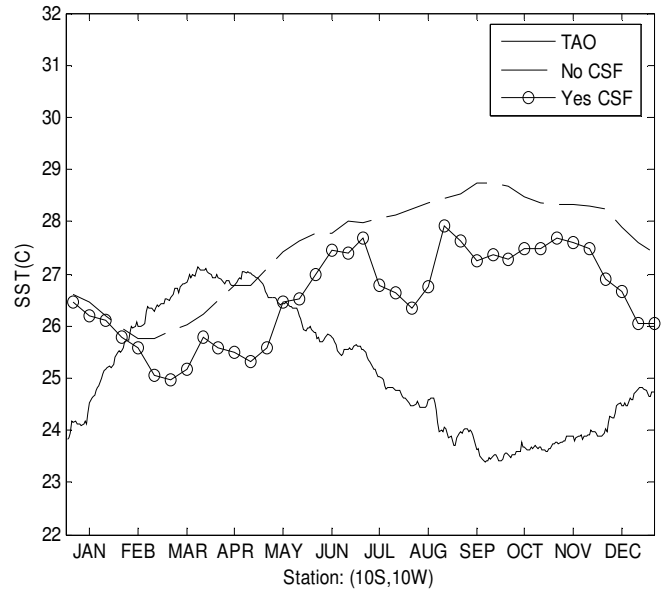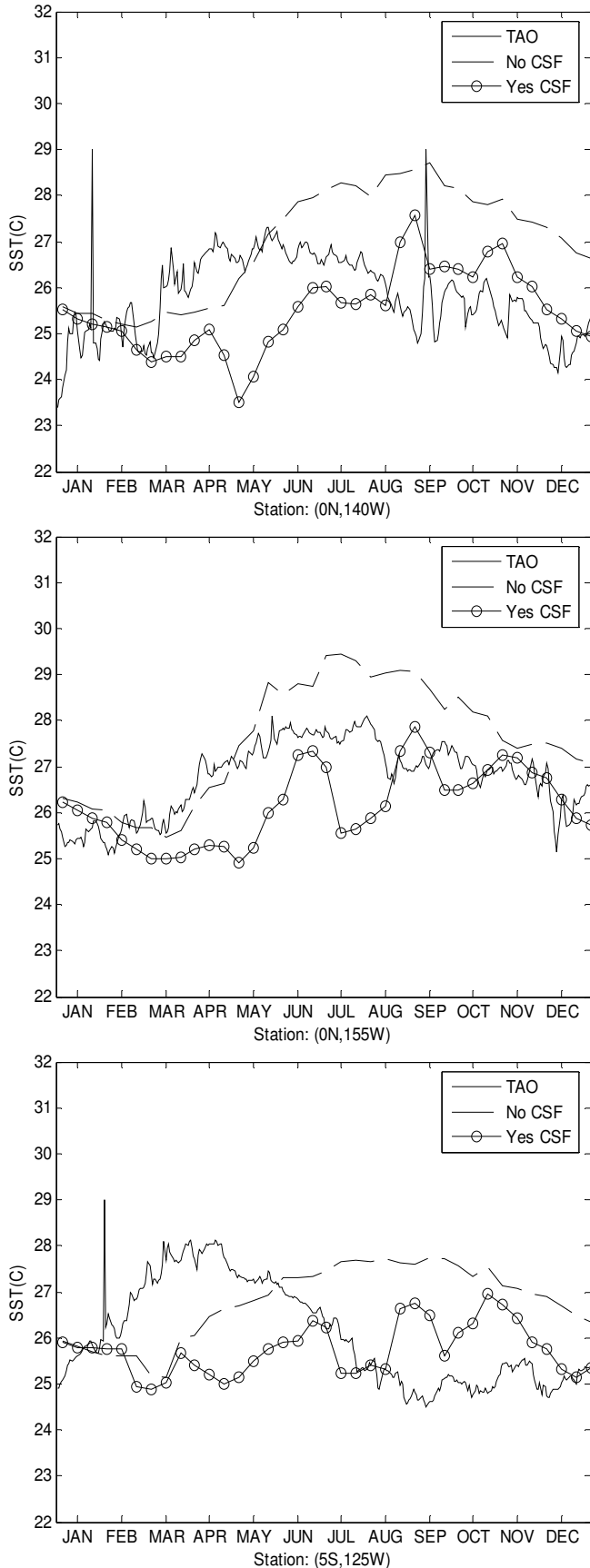Station: (5S,125W)

Station: (10S,10W)

Figure 8. Daily SST time series in 2001from TAO buoys (solid line), and those output from HYCOM simulations with CSF (cycle line) and without CSF (dash line) for 4 stations over Equatorial Pacific.

more sensitive to the boundary forcing. Moreover, the interaction between waves and currents might be more intensive in the strong eddy region. Deng et al. (2009) also demonstrated that the ocean surface currents are more sensitive to wind forcing in the low wind speed region than that in other regions. Since the wind direction is almost westward both in summer and winter over the Caribbean Sea and Gulf of Mexico, there is not much difference in the current structure among seasons in this region. The winds in summer are weaker than that in winter and the values of $\Delta \vec{T}_c$ in summer are also smaller than that in winter (Figure 7), suggesting that the changes in CSF-induced $\Delta \vec{T}_c$ are associated with the changes in wind speed.

VALIDATION AND DISCUSSION

MLD is partly determined by SST. The distribution of annual-mean Δthi and Δtem (Figures 3a, b, d, e, g and h) indicate that increased MLD tends to be accompanied with decreased SST. As an important parameter that can be used to verify the capability of a numerical model in simulating the upper ocean phenomena, SST can be directly measured with high accuracy by buoys. Tropical Atmosphere Ocean (TAO/TRITON) observational array data, which are updated every day, are freely available to the research community. Here, we use SST time series from TAO buoys which are deployed over the equatorial Pacific region to validate our simulation results. Figure 8

Table 2. Monthly-mean mixed layer thickness (for each site, the two lines list the simulation results without and with CSF, respectively), Site 1: (114.5°E, 17.5°N), site 2: (110.5°E, 8.5°N), site 3: (71.5°W, 36.5°N), site 4: (87.5°W, 24.5°N)).

	Unit: *m*	JAN	FEB	MAR	APR	MAY	JUN	JUL	AUG	SEP	OCT	NOV	DEC
Site 1	No csf	93.6	84.4	20.8	19.5	10.9	26.6	19.3	37.2	33.4	38	51.3	106.3
	Yes csf	94.3	86.9	22.8	22.4	12.1	16	18	40.2	46.7	44.8	95.3	119
Site 2	No csf	51.4	49.8	45	36.8	57.4	53.7	78.1	83	52.4	32.4	28.4	36.7
	Yes csf	51	53.2	43.3	37.2	51.3	56.3	76.3	75.1	58.1	38.8	35.2	30
Site 3	No csf	163.5	190.5	159.4	131.8	16.8	12.8	7.8	5.7	13.5	21.2	31.1	65
	Yes csf	163.4	208.6	289.4	125.1	15.5	12.5	7.1	6.5	16.2	23.3	27.8	83.5
Site 4	No csf	59.2	61.7	43.2	28.3	29	29.4	15.8	12.9	9.1	26.7	35.9	35.4
	Yes csf	59.6	61.9	43.4	38.4	19.7	31.9	12.4	13.9	13.2	37.4	32	40.4

displays the comparisons of SST from model simulation and from TAO observation performed on 4 sites. These are located at (0°N, 140°W), (0°N, 155°W), (5°S, 125°W) and (10°S, 10°W), respectively, covering the equatorial Pacific region sparsely. Considering no data assimilation applied in our modeling, the deviations between reproduced SSTs and observations are basically acceptable. All the four cases show that, in general, the results with CSF are decreased and slightly closer to observations comparing to that without CSF. CSF-induced improvements in SST simulation can be appreciated in almost all the seasons except spring.

However, it is currently inappropriate to conclude that the reproduced SST is substantially improved by the inclusion of CSF. Nevertheless, one certainty is that CSF is a necessary physics and is not negligible in upper ocean modeling, which is somewhat indicated by Figure 8. Kantha and Clayson (2004) argued that, the Langmuir cell-induced SST changes are well within the uncertainties in the modeled SST resulting from an imperfect knowledge of the air-sea flues used to drive the mixed layer models. Additionally, in our opinion, the imperfect mixed layer models are also partly responsible. It can also be found from Figure 8 that, the CSF resulted SST variations are quite pronounced during spring/summer periods (more than 1°C), and are relatively small in fall and winter when ML is thicker. Carniel et al. (2005) also found that, the surface wave (though through Langmuir cells and wave breaking) resulted SST differences are around 1°C.

As concluded earlier that CSF exerts more striking impacts on upper layer currents in eddy regions, we step further to discuss the influences of CSF on MLD in eddy regions. Table 2 lists the monthly-mean MLD for four sites which are all located in the eddy regions (site 1 is in north SCS, site 2 south SCS, site 3 north WNA, and site 4 is in Loop Current region). Results show that the ML is shallow in spring/summer and deeper in fall/winter. In other words, it presents a seasonal variability. CSF tends

to deepen the ML in every month except July. Previous studies (Kantha and Clayson, 2004; Carniel et al., 2005) found that Langmuir cells deepen the ML because of the increased mixing, and result in the drops of SST. Whereas, as a mediation of top boundary condition, CSF does not always tend to increase the MLD (or decrease the SST) over the whole model domain, but it does in eddy regions. The bigger changes in the eddy regions are probably resulting from the more intensive wave-current interaction reflected by the modulating of top boundary forcing in both momentum equation and ML model.

Conclusions

Ocean wave models and ocean current models are usually run independently, so that the impact of wave-current interactions on the ocean such as CSF is not included. In this study, a one-way coupling system consists of an ocean circulation model (HYCOM) and a wave model (WW3), is used to study the effects of CSF on ocean upper-layer dynamics including currents, temperature and upper-layer mixing. The CSF is calculated by wave variables derived from WW3, and is then imposed to HYCOM as an upper boundary condition. In order to verify the effects of CSF on upper ocean properties are consistent in different regions, experiments configured in three different regions (Global Ocean, SCS and WNA) with different horizontal resolutions (2.5°, 0.083° and 0.17°) are carried out to illustrate the details. The results are summarized as follows.

Only serving as a correction to the upper ocean boundary conditions, CSF can change the structures of current field by interacting with the mean currents as well as releasing TKE. The changes in ML current transport caused by CSF are comparable to wind-driven Ekman transport. The CSF-induced changes in annual-mean ML depth-integrated current transport $\Delta \vec{T}_c$ values are in the

range of 0 to 13 m^{2}s^{-1}, most of which are from 0 to 3 m^{2}s^{-1} and larger ones appear over the mid-latitude Westerly regions. The annual-mean changes in MLD Δthi are in the range of -15 to 80 m with obvious enhancement in the southern ocean. The annual-mean ML temperature Δtem are from -0.8 to 0.8℃. The magnitude of depth-integrated Stokes transport $\vec{T}_s$ is in the range of 0 to 2.2 m^{2}s^{-1}, which is in the same order as that of $\Delta\vec{T}_c$. However, for the most part of the global ocean, the directions of $\vec{T}_s$ are totally different from that of $\Delta\vec{T}_c$, except for the southern Westerly region. The CSF intensifies (reduces) the mixing in the ML, thus results in a decrease (an increase) in ocean surface temperature.

Similar to the global case, neither can CSF entirely change the structures of current pattern in the SCS experiments. The upper-layer basin-scale circulation of the SCS, which subjects to the monsoon system, is well simulated. The monthly-mean upper-layer circulation pattern of SCS varies with the monsoon winds. In general, it shows a distinct seasonal behavior which exhibits a strong cyclonic gyre in winter and a weak cyclonic gyre in the Northern SCS but an anti-cyclonic gyre in the southern SCS in summer. The CSF-induced annual-mean $\Delta\vec{T}_c$, Δthi, and Δtem in the ML of SCS vary from 0 to 5 m^{2}s^{-1}, -10 to 10 m, and -0.2 to 0.25℃, respectively. The monthly-mean $\Delta\vec{T}_c$ in the ML is changing month to month in both direction and magnitude.

The magnitudes of $\Delta\vec{T}_c$ are in the range of 0 to 30 m^{2}s^{-1}, but mostly within 0 to 3 m^{2}s^{-1}. The large values appear in the regions of intense gyre, which indicates that the CSF plays a more important role in those regions.

The main features of upper-layer circulation in WNA (Loop current, eddy-shedding and western boundary currents) are successfully simulated in comparison with other important studies. The rings shed episodically by Loop Current have a diameter of about 250 km and a westward propagation speed of $3\,km\cdot day^{-1}$. The CSF-induced annual-mean $\Delta\vec{T}_c$, Δthi, and Δtem in the ML of WNA vary from 0 to 27 m^{2}s^{-1} (with most less than 6 m^{2}s^{-1}), -20 to 30 m (with most from -10 to 10 m), and -0.4 to 0.4℃, respectively. The monthly-mean $\Delta\vec{T}_c$ in the ML of WNA also varies monthly in both direction and magnitude. The influences of CSF on $\vec{T}_c$ are most important in winter and least significant in summer. The CSF plays a significant role in regions where strong quasi-geostrophic flow presents.

In conclusion, although wave-induced CSF cannot fundamentally change the pattern of the ocean circulation, it still has a noticeable effect on ocean modeling, while unfortunately most ocean models do not consider such effects. With magnitude less than 5% of that of wind stress, CSF does not always increase the combined top stress; it also decreases the net stress when the wind and CSF are in opposite direction. CSF influences the upper layer properties, such as currents and SST, more pronounced in the eddy regions than in others; and the mixing in the eddy regions tends to be intensified in the presence of CSF, thus results in the increase of MLD. CSF draws important effects on upper layer currents over the Westerlies where strong wind waves present. The comparisons of SST with some available TAO buoy observations show that, the simulated SSTs with CSF are generally improved. However, it is now still hard to say that the model's SST reproduction skill is definitely improved, because the CSF-induced changes in SST are well within the uncertainties of external forcing and because of the imperfect knowledge of the parameterization of turbulent mixing. Nevertheless, the inclusion of CSF in ocean modeling is on the right way to develop a model for better representing the real ocean.

This study uses a one-way coupling which only investigates the effects of waves on currents, not vice versa. In the ocean, swells with wave length of more than 50 m commonly exist (indicated by our WW3 simulated results), and their directions are much different from that of the corresponding winds. Typically, Stokes depth is about 5 m in the open ocean (when the wave length is about 60 m), while under the same condition Ekman depth is much deeper (e.g. in 35°N, under a wind speed of 10 ms^{-1}, Ekman depth is ~120 m). So, in this context, it is valid to introduce the wave-induced CSF as a top boundary condition of the ocean circulation model. Different from the WNA case where the contributions of CSF to WBC can be found, in global case, the resolution is too coarse to resolve WBC, so we can not properly appreciate the contributions of CSF to WBC, while the effects of CSF on the ocean interior, such as Westerlies and Equatorial Ocean, can be appreciated clearly. Consistent results of experiments that conducted over three different domains (especially the two regional cases) indicate that our simulations are the representative of the real physics. One limitation of this study is that, we adopted 100% of the wind stress to the ocean circulation component, which is the common way used in ocean modeling at present. Actually, there must exist an energy partition depending on sea state between currents and waves; however, this partition still remains unknown. In order to represent the effects of waves here, we introduce the CSF as a correction to the wind stress.

ACKNOWLEDGEMENTS

REFERENCES

Ardhuin F, Jenkins AD (2006). On the interaction of surface waves and upper ocean turbulence. J. Phys. Oceanog., 36: 551-557.

Bleck R (2002). An Ocean General Circulation Model Framed in Hybrid Isopycnic-Cartesian Coordinates. Ocean Modeling, 4: 55-88.

Bye JAT (1967). The wave-drift current. J. Mar. Res., 25: 95-102.

Carder KL, Fanning KA, Betzer PR, Maynard V (1977). Dissolved silica and the circulation in the Yucatan Strait and the deep eastern Gulf of Mexico. Deep-Sea Res., 24: 49-60.

Carniel S, Sclavo M, Kantha LH, Clayson CA (2005). Langmuir cells and mixing in the upper ocean. IL NUOVO CLMENTO, 28: 33-54.

Chu PC, Edmons NL, Fan C (1999). Dynamical Mechanisms for the South China Sea Seasonal Circulation and Thermohaline Variablilities. J. Phys. Oceanogr., 29: 2971-2989.

Cochrane JD (1972). Separation of an anticyclone and subsequent developments in the Loop Current (1969). Texas A & M Univ. Ocean Studies. Eds: L. R. A. Capurro and J. L. Reid, Gulf Publishing Co., Houston, 2: 91-106.

Cooper CG, Forristall Z, Joyce TM (1990). Velocity and hydrographic structure of two Gulf of Mexico warm-core rings. J. Geophys. Res., 95: 1663-1679.

Deng Z, Wu K, Yu T (2007). The wave transport of the eastern area of the Pacific. ACTA OCEANOLOGICA SINICA (Chinese edition), 29(6): 1-9.

Deng Z, Wu K, Zhao D, Yu T (2009). Effects of Wind Waves of the Pacific Westerly on the Eastern Pacific Wave Transport. ACTA OCEANOLOGICA SINICA, 28(1): 83-88.

Fratantoni DM (2001). North Atlantic surface circulation during the 1990's observed with satellite-tracked drifters. J. Geophys. Res., 106: 22,067-22,093.

Hasselmann K (1970). Wave-driven inertial oscillations, Geophys. Fluid Dyn., 1: 463-502.

Huang NE (1979). On Surface Drift Currents in the Ocean. J. Fluid Mech., 91: 191-208.

Ianniello JP, Garvine RW (1975). Stokes transport by gravity waves for application to circulation models. J. Phys. Oceanog., 5: 47-50.

Kantha L, Clayson CA (2004). On the effect of surface gravity waves on mixing in the oceanic mixed layer. Ocean Modeling, 6: 101-124.

Kenyon KE (1970). Stokes transport. J. Geophys. Res., 75: 1133-1135.

Korvin-Kroukovsky YV (1972). Pure drift current and mass transport in coexistent waves. Deut. Hydro. Z., 25: 1-13.

Large WG, Mcwilliams JC, Doney SC (1994). Oceanic Vertical Mixing: A Review and a Model with a Nonlocal Boundary Layer Parameterization. Rev. Geophysics, 32: 363-403.

Liu Q, Kaneko A, Su J (2008). Recent Progress in Studies of the South China Sea Circulation, J. Oceanography, 64: 753-762.

Mcwilliams JC, Rsetrepo JM (1999). The wave-driven ocean circulation. J. Phys. Oceanogr., 29: 2523-2540.

Mcwilliams JC, Sullivan PP, Moeng CH (1997). Langmuir turbulence in the ocean. J. Fluid Mech., 334: 1-30.

Metzger EJ, Hurlburt H (1996). Coupled Dynamics of the South China Sea, the Sulu Sea, and the Pacific Ocean, J. Geophys. Res., 101: 12331-12352.

Ochoa J, Sheinbaum J, Baden A, Candela J, Wilson D (2001). Geostrophy via Potential vorticity inversion in the Yucatan Channel, J. Mar. Res., 59: 725-747.

Oey LY, Ezer T, Lee HC (2005). Loop Current, Rings and Related Circulation in the Gulf of Mexico: A Review of Numerical Models and Future Challenges. Geophysical Monography Series, 161: 31-56.

Polton JA, Lewis DM, Belcher SE (2005). The role of wave induced Coriolis-Stokes forcing on the wind-driven mixed layer, J. Phys. Oceanogr., 35: 444-457.

Qu T (2000). Upper layer circulation in the South China Sea, J. Phys. Oceanogr., 30: 1450-1460.

Romanou A, Chassignet EP, Sturges W (2004). The Gulf of Mexico circulation within a high resolution numerical simulation of the North Atlantic Ocean. J. Geophys. Res., 109, CO1003, doi: 10.1029/2003CJ001770.

Shaw PT, Chao S (1994). Surface circulation in the South China Sea. Deep-Sea Res., 41: 1663-1683.

Sturges W, Leben R (2000). Frequency of ring separations from the Loop Current in the Gulf of Mexico: A revised estimate, J. Phys. Oceanogr., 30: 1814-1818.

Teixeira MAC, Belcher SE (2002). On the distortion of turbulence by a progressive surface wave, J. Fluid Mech., 458: 229-267.

Vukovich FM (1995). An updated evaluation of the Loop Currents eddy shedding frequency. J. Geophys. Res., 100: 8655-8659.

Wu K, Liu B (2008). Stokes drift-induced and direct wind energy inputs into the Ekman layer within the Antarctic Circumpolar Current. J. Geophys. Res., 113, C10002, doi: 10.1029/2007JC004579.

Wyrtki K (1961). Scientific results of marine investigation of the South China Sea and Gulf of Thailand. NAGA Report, 2: 195.